La Salle University
La Salle University Digital Commons

Environmental Science Faculty Work | Environmental Science

12-8-2021

Quantification of mineral reactivity using machine learning interpretation of micro-XRF data

Julie J. Kim

Florence Ling

Dan A. Plattenberger

Andres F. Clarens

Catherine A. Peters

Follow this and additional works at: https://digitalcommons.lasalle.edu/enviro_sci_faculty

 Part of the Environmental Sciences Commons, and the Geochemistry Commons

Applied Geochemistry 136 (2022) 105162

Contents lists available at ScienceDirect

Applied Geochemistry

journal homepage: www.elsevier.com/locate/apgeochem

Quantification of mineral reactivity using machine learning interpretation of micro-XRF data

Julie J. Kim [a], Florence T. Ling [b], Dan A. Plattenberger [c], Andres F. Clarens [c], Catherine A. Peters [a,*]

[a] Department of Civil and Environmental Engineering, Princeton University, Princeton, NJ, 08544, USA
[b] Department of Chemistry, Environmental Science Program, La Salle University, Philadelphia, PA, 19142, USA
[c] Engineering Systems and Environment, University of Virginia, Charlottesville, VA, 22904, USA

ARTICLE INFO

Handling editor: Dr.Z Zimeng Wang

Keywords:
SMART mineral mapping
Mineral classifier
Synchrotron XRF
Reactive transport modeling
Machine learning
Shale

ABSTRACT

Accurate characterizations of mineral reactivity require mapping of spatial heterogeneity, and quantifications of mineral abundances, elemental content, and mineral accessibility. Reactive transport models require such information at the grain-scale to accurately simulate coupled processes of mineral reactions, aqueous solution speciation, and mass transport. In this work, millimeter-scale mineral maps are generated using a neural network approach for 2D mineral mapping based on synchrotron micro x-ray fluorescence (μXRF) data. The approach is called Synchrotron-based Machine learning Approach for RasTer (SMART) mapping, which reads μXRF scans and provides mineral maps of the same size and resolution. The SMART mineral classifier is trained on coupled μXRF and micro-x-ray diffraction (μXRD) data, which is what distinguishes it from existing mapping tools. Here, the SMART classifier was applied to μXRF scans of various sedimentary rock samples including consolidated shales from the Eagle Ford (EFS1), Green River (GRS1), Haynesville (HS1), and New Albany (NAS1) formations and a syntaxial vein from the Upper Wolfcamp formation. The data were obtained using an x-ray microprobe at beamline 13-ID-E at the Advanced Photon Sources. Individual mineral maps generated by the SMART classifier well-captured distributions of both dominant and minor phases in the shale rocks and revealed EFS1 and GRS1 to be carbonate rich shales, and NAS1 and HS1 to be sulfide rich shales. The EFS1 was further characterized for its trace mineral abundances, grain sizes, trace element composition, and accessibility. Approximately 4.4 wt% of the rock matrix were found to be pyrite, with a median grain size of 3.17 μm in diameter and 62% of the grains predicted to be smaller than 4 μm. Quantifications of trace elements in pyrite revealed zinc concentrations up to 4.2 wt%, along with minor copper and arsenic copresence. Mineral accessibility was examined by contact with other phases and was quantified using a new type of image we are calling an adjacency map. Adjacency analyses revealed that of the total pyrite surface present in the EFS1, 28% is in contact with calcite. The adjacency maps are useful for quantifying the likelihood that a mineral could be exposed to fluids after dissolution of a contacting reactive phase like calcite. Lastly, pooling data from different samples was demonstrated by training a classifier using two sets of coupled μXRF-μXRD data. This classifier yielded an overall accuracy of >96%, demonstrating that data pooling is a promising approach for applications to a wide suite of rock samples of different origin, size, and thickness.

1. Introduction

Visualizing the spatial patterns of minerals in sedimentary geologic media is essential to characterizing reactivity and associated properties of porosity, permeability, wettability, toxicity, strength, and texture. The ability to mineralogically map millimeter-scale areas with micrometer scale resolution is especially important in the context of surficial and subsurface processes such as CO_2 sequestration, hydraulic fracturing, geothermal energy production, nuclear waste management, solid mine waste management, and groundwater quality control. Reactive transport models are used to describe relevant geochemical reactions and transport processes in these systems (Deng et al., 2021), and modeling efforts rely on characterization of mineral reactivity including information about the elements and minerals that are present and their

* Corresponding author.
E-mail address: cap@princeton.edu (C.A. Peters).

https://doi.org/10.1016/j.apgeochem.2021.105162
Received 6 October 2021; Received in revised form 2 December 2021; Accepted 3 December 2021
Available online 8 December 2021
0883-2927/© 2021 The Authors. Published by Elsevier Ltd. This is an open access article under the CC BY-NC-ND license (http://creativecommons.org/licenses/by-nc-nd/4.0/).

abundances, spatial and size distributions, and extent of accessibility. Furthermore, the ability to resolve mineral characteristics down to grain-scales is critical because in geologic media like sedimentary rocks, reaction kinetics and mass transport processes are operative at these scales (Baek et al., 2019; Crandell et al., 2012; Ma et al., 2021).

There is further motivation to not only identify and map the minerals but also have a way of elementally characterizing the mineral phases as minerals in natural environments serve as host phases to foreign and critically important elements with regard to toxicity or value (Hunter et al., 2020; Ling et al., 2018). It has also been observed that fluid-rock interactions can cause reactive minerals to dissolve and expose toxic element-bearing mineral phases such as pyrite, leading to liberation of toxic or critical elements such as arsenic that can cause serious environmental concerns (Deng et al., 2020; Kreisserman and Emmanuel, 2018; Zhang et al., 2017). Other literature have found that elemental composition, stoichiometry of elements, or incorporation of foreign ions dictate the kinetics of reactions (Glynn et al., 1990), further motivating the need to identify and quantify chemically heterogeneous minerals in many environmental engineering and earth sciences contexts.

There have been many advancements in mineral characterization utilizing x-ray or electron-based imaging techniques in 2D and in 3D (Asadi and Beckingham, 2021; Beckingham et al., 2016; Ellis and Peters, 2016; Lai et al., 2015; Landrot et al., 2012; Peters, 2009; Qin and Beckingham, 2021). The aforementioned literature demonstrate that with maps of minerals, quantification and localization of mineral phases, quantification of grain sizes as well as differentiation of reactive and non-reactive minerals are possible. These efforts also highlight that many decisions about model resolution and spatial averaging can be obtained from spatial visualization of minerals. Other literature have highlighted the significance of accurate mineral descriptions on the evolution of solution chemistry, effective reaction rates, extent of mechanical deformation or fracture propagation (Glassley et al., 2002; Li et al., 2006, 2007; Liu et al., 2017; Spokas et al., 2018). With fast advancements in synchrotron-based techniques that enable resolution of micron- and even nano-meter scales, there remains opportunities to improve mineral mapping and reactivity characterizations. Synchrotron-based 2D element maps are readily generated by microprobe beamlines and carry valuable information to characterize elemental stoichiometry, content and distribution. With machine learning, we are extending these capabilities to characterize not just elements but also mineral features.

This work provides new applications of a recently-developed tool for 2D mineral mapping based on synchrotron μXRF data, i.e., Synchrotron-based Machine learning Approach for RasTer (SMART) mineral mapping (Kim et al., 2021). Briefly, the SMART mineral classifier is a neural network trained on a coupled micro x-ray fluorescence (μXRF) and micro x-ray diffraction (μXRD) dataset. Once trained, the classifier can be applied directly to new μXRF data to predict the minerals. Because of its use of XRD data in the training data, the SMART classifier brings a critical improvement to existing tools because of the potential to differentiate minerals of similar chemistry, stoichiometry, or minerals with impurities. Conventional methods of spatial mapping are unable to map multimineral presence in a single pixel and the SMART classifier approach is distinguished from existing methods for this capability. For a comprehensive review of other methods and recent advancements for 2D mapping, see Kim et al. (2021). With the application of the SMART classifier to extract mineralogical information from μXRF scans, synchrotron x-ray microprobes now carry even more value and potential to improving descriptions of mineral reactivity.

This work utilizes methodologies presented in Kim et al. (2021) and goes beyond to demonstrate complex applications of SMART mineral classification including qualitative and quantitative interpretations of mineral maps for improved mineral reactivity descriptions. While that prior work presented new application such as classifier training and upscaling, this work details ways in which 2D mineral maps can provide descriptions such as abundances, trace element presence, grain sizes, and accessibilities in fine-grained materials. Here, we trained a SMART mineral classifier on a new dataset compiled from two rock sources, and we evaluated performance on a known dataset from a sample of the Eagle Ford shale. The newly trained SMART classifier was then applied to scans of four other natural rock samples of different origins to demonstrate the power of this machine learning method in generating mineral maps from μXRF scans for which no μXRD data were collected. The remainder of the paper focuses on the Eagle Ford shale to quantify trace element composition and identify its host mineral phase using the generated mineral maps. An analysis of the grain size distribution was done for pyrite in the Eagle Ford sample, which required stereology to extract this 3D information from 2D images. Regarding mineral accessibility, we introduce mineral adjacency as a new definition of mineral accessibility that is appropriate for consolidated geologic media such as shales. We have defined this not by access to pore-space fluids, as is the norm for porous granular material, but by contact with a mineral phase that may dissolve away. To achieve this, a new type of 2D representation called an adjacency map is presented, where mineral contact lines are delineated, and specific surface areas are calculated.

2. Rock samples

In this work, five different sedimentary rock samples were characterized. One shale originates from the Eagle Ford formation, which spans southeastern Texas. The Eagle Ford shale sample (EFS1) is characterized in detail because its high carbonate content makes it susceptible to hydrologic and mechanical property changes (Spokas et al., 2019), and because of the fine scale distribution of sulfide phases within matrices of silicate minerals (Deng et al., 2020). A sample originating from the Upper Wolfcamp formation (UW1) of Texas was also studied in an attempt to characterize the mineralogy of a wide syntaxial carbonate vein. Additional characterizations and 3D xCT images of the UW1 sample are provided elsewhere (Peters et al., 2021). Three other shale samples were studied: Green River shale (GRS1) underlying Colorado, Wyoming, and Utah, New Albany shale (NAS1) of the Illinois basin, and Haynesville shale (HS1) underlying Arkansas, Texas, and Louisiana. This suite of rock samples is ideal for demonstration of upscaling capabilities and direct applicability of the SMART method because of the variability in sample sizes, thickness, and granular sizes. Fig. 1 presents images of some of the samples prior to sectioning and the images show unique textural features of each rock sample. The EFS1 and UW1 thin sections were prepared by Spectrum Petrographics (Vancouver, WA), and the GRS1, NAS1, and HS1 samples were prepared as polished thick (~mm)

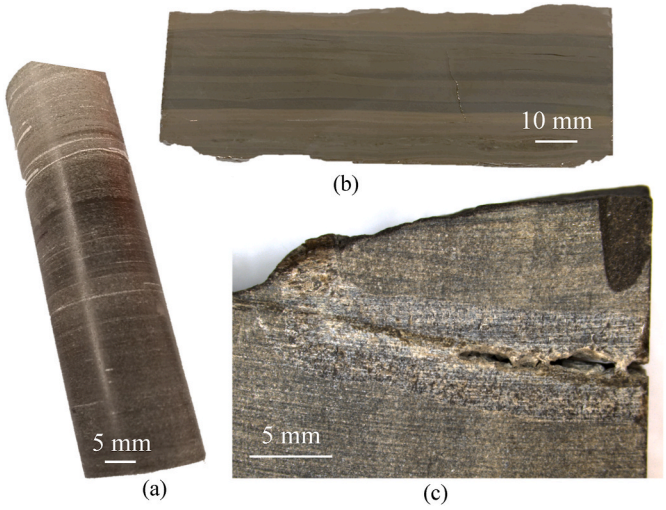

Fig. 1. Sample images of select rock samples studied prior to thin sectioning: (a) EFS1 core; (b) GRS1 slab; (c) UW1 bulk sample showing the horizontal vein with intermittent void space.

samples.

3. Methods

3.1. Synchrotron μXRF data acquisition and analysis

All synchrotron experiments were performed at the hard x-ray microprobe, beamline 13-ID-E, at the Advanced Photon Source (Lanzirotti et al., 2016; Sutton et al., 2017). The incident energy was set to 17.5 keV for UW1, and 18 keV for EFS1, GRS1, HS1, and NAS1. The μXRF data were collected in raster scanning mode using a high-speed silicon drift diode detector located 90° to the incident beam. Dwell times for the μXRF scans ranged from 20 ms to 100 ms. The scans sizes and resolutions are as follows: EFS1 scan was 500 μm by 500 μm with pixel resolution of 2 μm, UW1 scan was 6 mm by 4.4 mm with pixel resolution of 5 μm, GRS1 scan was 0.5 mm by 8.4 mm with pixel resolution of 3 μm, HS1 scan was 0.5 mm by 10 mm with pixel resolution of 3 μm, and NAS1 scan was 0.8 mm by 8 mm with pixel resolution of 3 μm. For GRS1, HS1, and NAS1, the long dimension was perpendicular to the sedimentary bedding plane. For the scan of EFS1, μXRD data was also collected for neural network training.

To generate individual element maps, the XRF intensity data is used directly, without the machine learning algorithm. Analyses were performed using LARCH: GSE Mapviewer (Newville 2013), and the resulting element maps have color gradients that are representative of concentrations.

To approximate weight percentages of trace elements, NIST SNRLXRF was used to interpret μXRF data at select pixels. Theoretical fluorescence intensities of a range of compositions were calculated and calibration curves were built to estimate weight percentages. In this work, the focus was on quantifying trace elements in pyrite and calcite. See the Supplementary Material and Deng et al. (2020) for details.

3.2. SMART training and application

One of the research objectives was to compare performance of two SMART mineral classifiers trained on different data sets. One was trained on the coupled μXRF-μXRD data set from EFS1, and one was trained on a dataset that combined EFS1 with data from a scan of a mixture of mineral standards (which we call 'mineral mixture'). Both of these datasets are introduced elsewhere (Kim et al., 2021), but using them as a pooled dataset for neural network training is new in this work. The mineral mixture is composed of 6 standards including calcium carbonates, iron sulfides, and manganese oxides. See the Supplementary Material for element maps from the mineral mixture sample. The purpose of this mixture was to introduce mineral phases with similar stoichiometric ratios (pyrite and pyrrhotite) and with similar elemental makeup (calcite, aragonite, and dolomite). Dolomite is not the same chemical formula as calcite and aragonite, but the magnesium is not detectable in a beamline that uses hard x-rays, so the μXRF data appear to be similar.

In a SMART training data set, each data point consists of an XRF spectrum interpreted as fluorescence intensities of 8 elements (listed in Table 1) and an XRD diffraction pattern interpreted in terms of presence or absence of 26 possible minerals, which included carbonates, sulfides, oxides, and silicates. The μXRD analyses in the pixels selected for the original training data set for EFS1 revealed three dominant minerals (Table 1) and therefore the EFS1-trained SMART classifier is capable of identifying and mapping only these three minerals. This classifier was intended to be applied for self-similar upscaling to larger μXRF scans of Eagle Ford shale. Total of 6 mineral phases were identified in the mineral mixture sample (Table 1) and of those minerals, two overlapped with the minerals originally identified in EFS1. Combining these datasets, a total of 7 minerals could be identified using the SMART classifier trained on the pooled data. Details about training with this pooled dataset, error evolution, and the stopping criteria set to minimize overfitting can be found in the Supplementary Material. The μXRF scans of UW1, GRS1, NAS1, and HS1 were interpreted by applying the classifier trained on the pooled data, taking into account differences in the sample thickness and incident energy among different samples.

Table 1
Summary of training data sets from EFS1 and from the pooled data (EFS1 and mineral mixture).

	EFS1 training data	Pooled training dataset
Elements	Sulfur	Sulfur
	Potassium	Potassium
	Calcite	Calcite
	Titanium	Titanium
	Manganese	Manganese
	Iron	Iron
	Arsenic	Arsenic
	Strontium	Strontium
Minerals	Calcite ($CaCO_3$)	Calcite ($CaCO_3$)
	Pyrite (FeS_2)	Aragonite ($CaCO_3$)
	Quartz (SiO_2)	Dolomite ($(Ca,Mg)(CO_3)_2$)
		Pyrite (FeS_2)
		Pyrrhotite (FeS)
		Pyrolusite (MnO_2)
		Quartz (SiO_2)
Number of training pixels	192	472

In a mineral map, for each pixel, j, the raw output of the SMART mineral classifier (P) is a continuous variable between 0 and 1 for each mineral i, and the value, P_{ij}, is representative of the likelihood of presence of that mineral. To generate individual mineral maps, this continuous variable is plotted as a color gradient in every pixel. As a result, 7 individual mineral maps, each with the same pixel resolution as the original μXRF scans, were generated EFS1 and UW1. To generate a multimineral map, where only one mineral is allowed for each pixel, P_{ij} were examined, and the largest value indicated the mineral assigned to that pixel. Multimineral maps are presented for EFS1, GRS1, NAS1, and HS1.

3.3. Abundance estimates and quantitative powder XRD analysis

Abundance estimates for the minerals identified via the SMART classifier were determined from P_{ij} values. The total volume fraction, F_i, for each mineral phase was calculated by

$$F_i = \frac{1}{N}\sum_{j=1}^{N}\frac{P_{ij}}{\sum_{i=1}^{m}P_{ij}} \quad (1)$$

where m is the total number of minerals, and N is the total number of pixels. Note that for randomly oriented objects, area fractions in 2D images are representative of volume fractions in 3D, according to the principle of Delesse (Weibel, 1989). The volume fractions were converted to weight fractions using the respective densities of each mineral phase. For EFS1, these weight fractions were compared to quantitative powder XRD data for a larger sample of the rock (Kim et al., 2021).

For the GRS1 sample scanned without μXRD data collection, separate powder XRD analyses were conducted for the purpose of comparing with results of the mineral classifier. Bruker D8 Advance X-Ray diffractometer with Ag Kα radiation (wavelength of 0.559 Å) was used to collect the diffraction data between a two-theta range of 3°and 20° with a step-size of 0.025°. Post analysis was done using the peak matching software DIFFRAC.EVA. The labelled XRD pattern can be found in the Supplementary Material.

3.4. Pyrite grain size distributions

In models of mineral reactivity, grain size distributions are needed to guide decisions on model resolution and for potential application to higher dimensional modeling. To demonstrate how 2D mineral maps

can be used to predict the grain size distribution of pyrite, we employed principles of stereology (Sahagian and Proussevitch, 1998), which is a means of generating 3D interpretations of materials using 2D imaging. Using the individual pyrite mineral map for EFS1, the area of each pyrite object was determined by pixel counting and assigned an equivalent circle diameter. To extrapolate to 3D, we assumed a simple polydisperse system of spheres to represent the grains. Determination of the corresponding spherical objects is based on using the probability of cross-sections originating from a sphere of a particular size. This is necessary because a 2D plane cuts through any possible slice of a sphere that it intersects, and a probabilistic approach is needed to assign sphere diameters to the 2D circular objects. In this work, geometric class sizes were selected, where each interval is smaller by a factor of $10^{-0.1}$. It is important to note that the assumption of spherical particles may not closely represent reality, however, this assumption may be reasonable as pyrite phases are often found as framboids in sedimentary rocks (Kreisserman and Emmanuel, 2018; Liu et al., 2019). It is also important to recognize the potential for underestimation of the number grains of smaller sizes when assuming a spherical shape (Sahagian and Proussevitch, 1998), but results still gave valuable insights into approximate size distributions of pyrite.

3.5. Pyrite accessibility and quantification of specific surface areas

Accessibility was analyzed via generation of adjacency maps derived from individual mineral maps. Each pixel at the boundary of a mineral is distinguished based on what mineral phase it is contacting, and the total perimeter line lengths are apportioned by pixel counting. This analysis is independent from the grain size analysis, and there are no assumptions of spherical grains.

Total specific surface areas for calcite and pyrite were also calculated. The surface area values here are different from the conventional quantity of surface area in sedimentary media which quantifies contact with pore space (or the fluid phase). Here, surface area of a mineral phase is the surface of the mineral adjacent to other minerals. The approach is as follows. The 2D adjacency maps are used to calculate a mineral's perimeter density value which is the total mineral perimeter length divided by that mineral's total image area, yielding a value with units of inverse length. If one imagines integrating sequential 2D planes through a 3D medium, the perimeter density is an estimation of the mineral's total boundary surface area divided by the total mineral volume, which is called specific surface area and has units of inverse length. In this work, a range was reported to account for the pixelation of boundaries and the fact that the correct length might be the pixel length, or it might be the hypotenuse, or anything in between. The specific surface area values are presented here in conventional units of m^2/g, using densities of the mineral phases.

This analysis is discussed in this paper in the context of mineral accessibility. On the principle that carbonate phases are soluble, especially in acidified solutions, we ultimately sought to quantify the amount of pyrite surface that is in contact with calcite as opposed to quartz.

4. Results and discussion

4.1. Demonstration of mineral classifier applications and mapping capabilities

In this section, we present the results of application of the pooled-data-trained SMART classifier to the EFS1 scan to assess improvements in mineral characterizations. The pooled-data-trained classifier was found to have an exceedingly low misclassification rate of $<4\%$ for all minerals included here. See Supplementary Material for a summary of the misclassification rates and quantifications of false predictions for each mineral phase. Compared to the EFS1-trained classifier performance, calcite misclassification rate decreased by 1% while pyrite misclassification rate increased by 1.5%. Such small changes conclude neither a significant improvement nor a decline in the classifier performance, and visual comparison of maps generated from the EFS1-trained classifier and the pooled-data-trained classifier did not yield any major differences. One notable improvement is in the additional identification of dolomite in the Eagle Ford shale (Fig. 2), which was not captured in the self-similar analysis of EFS1 using the original EFS1-trained classifier (Kim et al., 2021). The presence of dolomite training data from the mineral mixture has allowed for identification of dolomite in EFS1, which was likely to have been labelled as calcite using EFS1-trained classifier. This shows prospects for utilization of mineral standards to expand on the number of identifiable minerals. Combining information from the individual mineral maps and the multimineral map (Fig. 2), it can be seen that the calcite areas are mostly homogeneous and the other areas containing quartz are more mineralogically heterogeneous, embedding phases like dolomite or pyrite. Aragonite, pyrrhotite, and pyrolusite presence appear to be negligible in the EFS1.

Here we also present the mineral mapping and element characterizations for the vein sample (UW1) using the pooled-data-trained classifier. A grayscale image highlights many features of the vein area (Fig. 3a) and the SMART-generated mineral maps are also presented in Fig. 3. The mineral maps of 5 μm resolution reveal a vein that is a former fracture filled with calcite, quartz, and large dolomite crystals. Pyrite grains are observed to be scattered throughout the inner and outer matrices of the vein. Elemental data from the μXRF scans were examined together with the dolomite- and calcite-labelled regions, and it was concluded that most of the iron is in the dolomite crystals (ferroan dolomite), and to a lesser extent in the calcite. NIST NRLXRF-based quantifications of the extent of iron incorporation in the carbonates revealed approximately 0.3 wt% in the slightly iron rich regions and upto 22 wt% in the highly iron rich regions.

Additionally, as seen in Fig. 3h, the remaining void content in the vein was distinguished in UW1. A secondary thresholding step of the classifier output for quartz, which involved separating out two groups of pixels, was conducted. This was done in order to identify locations of the void space, which was informed via absence of detectable elements. Although initially predicted as quartz by the classifier, this false prediction is most likely due to lack of training data on blank or empty pixels. While the SMART classifier is not a suitable tool for void or pore space segmentation, the probable areas of empty pixels can be distinguished via secondary thresholding of the classifier output.

Application of the pooled-data-trained SMART classifier to three other shale samples is shown in Fig. 4. The dominant element map for each rock sample is presented to complement the multimineral map (Fig. 4b, 4f, 4h). The multimineral maps reveal that the GRS is dominated by dolomite, with presence of other commonly found minerals such as pyrite or calcite (Fig. 4a). This characterization agrees well with minerals identified in the powdered XRD data obtained from a different location of the Green River shale core (Supplementary Material) and are in line with the minerals identified in this particular geologic formation. It is however also likely that this fine-grained sedimentary rock contains other minerals not listed in Fig. 4, as the powder XRD indicates presence of other minerals like analcime or chalcopyrite. The XRF scans also revealed presence of trace elements such as Ti, Sr or As, which may be hosted by these unidentified mineral phases. Two other shales, NAS1 (Fig. 4e) and HS1 (Fig. 4g) exhibited dominance of iron, calcium, and manganese rich mineral fractions, and iron rich mineral fractions, respectively. Both NAS1 and HS1 exhibit the expected fine-grained nature of shales, while HS1 embeds larger grains of dolomite throughout the shale matrix. The ability to obtain multi-millimeter mineral maps with the same resolution as the original scan within seconds and without additional training data or XRD data collection is clearly an improvement to existing methods of spatial characterization.

4.2. Quantification of mineral abundances

Quantification of the mineral abundances revealed that the EFS1 is

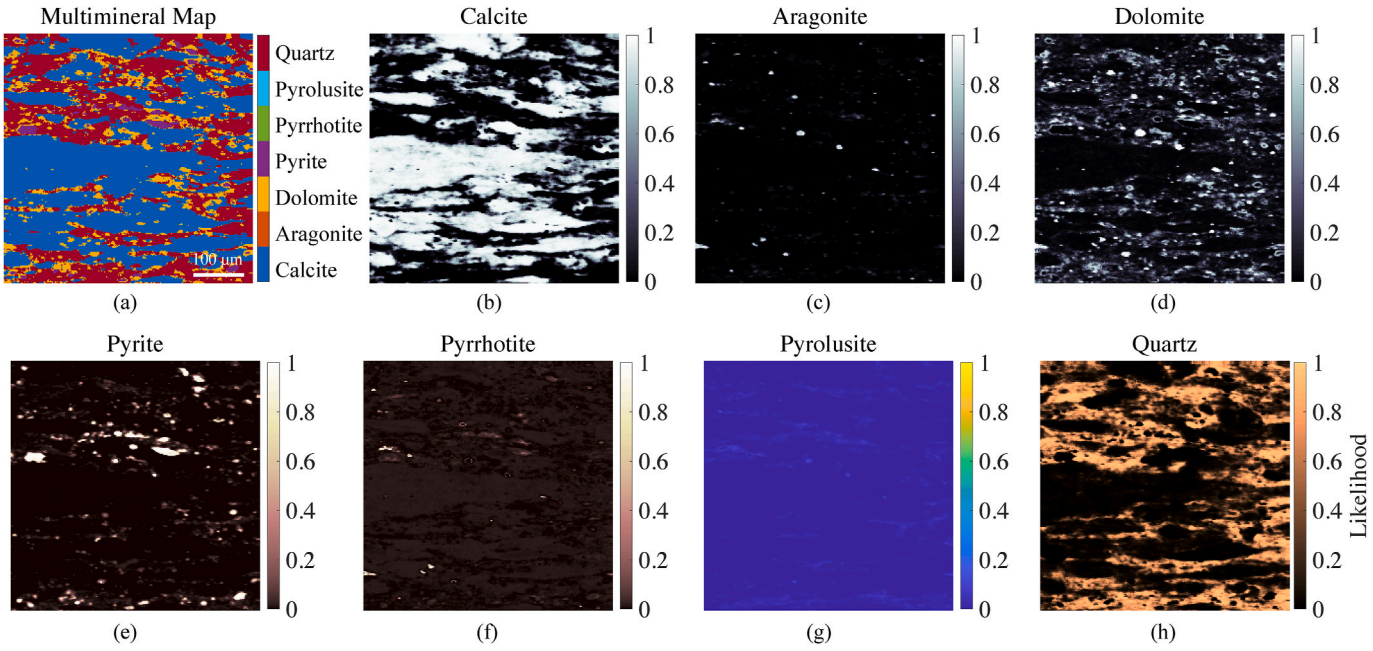

Fig. 2. Mineral maps of EFS1 of size 500 μm by 500 μm generated using the SMART classifier trained on the pooled data. (a) Generated 2 μm resolution multimineral map, where only one phase is assigned for a single pixel, and (b–h) carbonates, sulfides and manganese oxide maps for individual minerals. Each mineral category uses a unique color bar and the color bar indicates likelihood of presence. (For interpretation of the references to color in this figure legend, the reader is referred to the Web version of this article.)

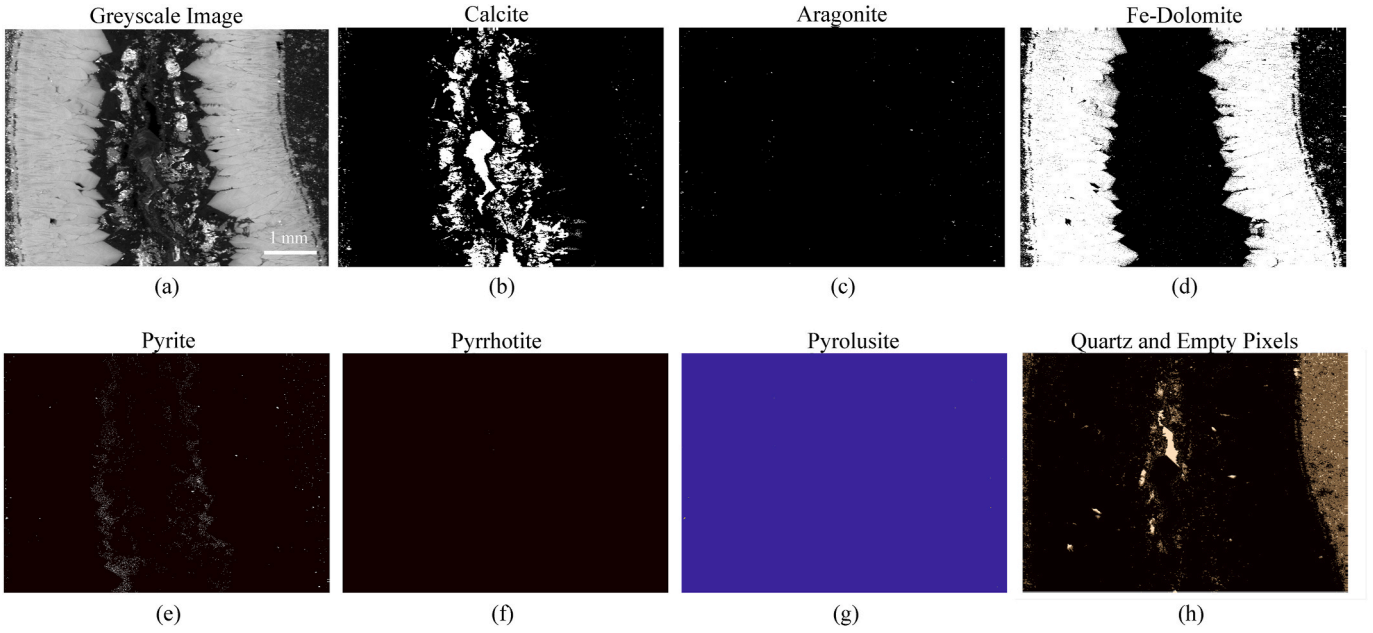

Fig. 3. UW1 mineral maps of size 6 mm by 4.4 mm generated using the pooled-data-trained classifier. (a) A grayscale image showing distinct mineral features of the vein which is approximately 5 mm wide, and (b–h) individual mineral maps of 7 minerals (5 μm resolution). In (h), for quartz, the brightest spots show the probable locations of the pore space (empty pixels) distinguished based on a secondary thresholding step.

calcite and quartz rich, and contains approximately 4.4 wt% pyrite (Table 3) and other sulfide and carbonate minerals. For pyrite, the predicted weight fraction is higher than the pyrite weight fraction estimated by powder XRD, and differences may be due to comparison of weight fractions from different parts of the rock sample or due to the detectable limit of laboratory powder XRD. By comparison, an aggregate calculation of pyrite in the more conventional multimineral map (Table 2), where only one mineral presence is allowed for each pixel, revealed underestimation of the mineral abundance. This is likely due to the higher probability of calcite or quartz presence in each pixel in this carbonate- and silicate-rich shale rock, which led to missing nearly half of pyrite copresence. All other minor phases (i.e., aragonite, pyrrhotite, and pyrolusite) were also completely missed in the multimineral case, indicating that multimineral maps are more susceptible to underestimation of mineral phases presence, especially those that are masked or surrounded by more dominant phases. Small discrepancies in the weight fractions can be considered within error of the analysis; however, detailed elemental analyses may reveal motivation to capture even the

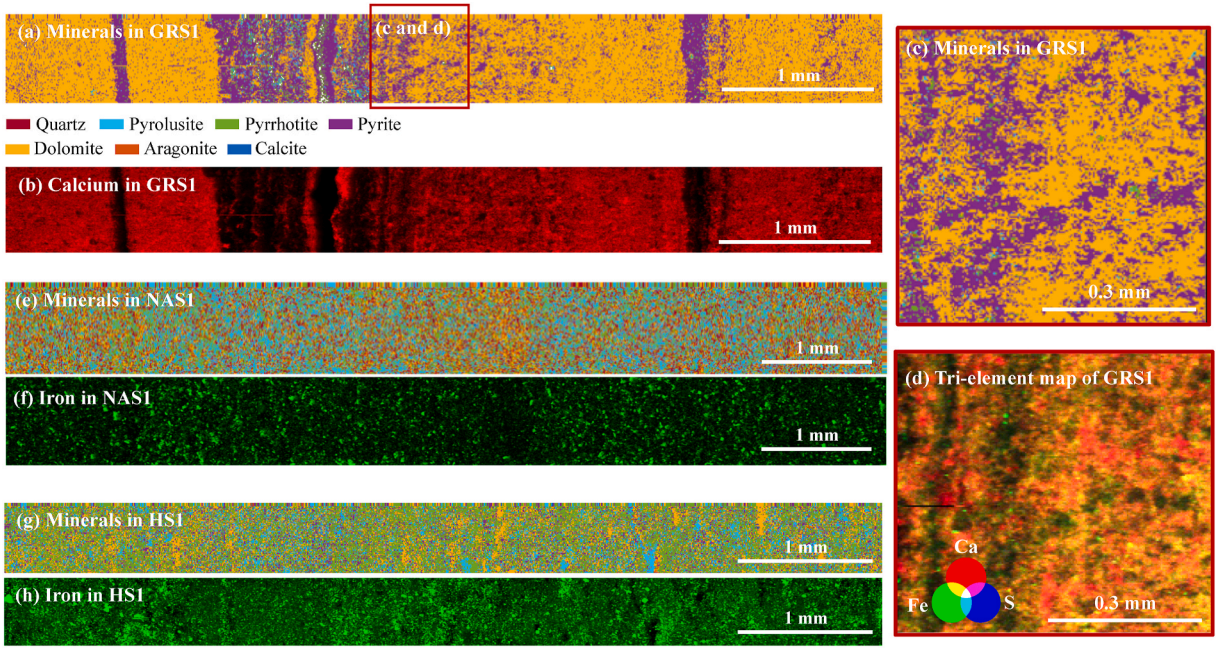

Fig. 4. Multimineral maps of (a) GRS1 (e) NAS1 and (g) HS1, and select element maps of (b) calcium from GRS1, (f) iron from NAS1, and (h) iron from HS1. Mineral maps of GRS1 and HS1 have been truncated and do not depict the full length of the original scans. Right two panels (c) and (d) are close-up mineral and element maps from the boxed area of GRS1, respectively, capturing fine scale distribution of minerals and calcium, iron, and sulfur in the rock.

Table 2
Quantification of minerals as weight percentages obtained via different mineral maps from the EFS1 scan. Also included are powder XRD analyses of a specimen from the Eagle Ford rock sample.

	7 individual mineral maps	Multimineral map (one mineral per pixel)	3 individual mineral maps	Powder XRD
Aragonite	1.2%	0%	–	
Calcite	46%	52.8%	58.2%	70.7%
Dolomite	16.4%	12.1%	–	
Pyrite	4.4%	2.1%	2.9%	1.4%
Pyrrhotite	2.1%	0%	–	
Pyrolusite	0.7%	0%	–	
Quartz	29.1%	33.0%	34.4%	25.8%
Unidentified/ Kaolinite	–	–	4.4%	2.1%

Table 3
Quantification of minerals as weight percentages obtained for different rock samples.

	Vein sample	Shale rock samples		
	UW1	GRS1	NAS1	HS1
Calcite	13.9%	15.2%	3.1%	2.0%
Aragonite	2.0%	11.8%	11.4%	11.9%
Dolomite	47.7%	23.3%	9.9%	10.3%
Pyrite	11.6%	41.6%	26.5%	23.8%
Pyrrhotite	6.1%	3.2%	18.5%	21.0%
Pyrolusite	0.5%	4.8%	29.7%	29.4%
Quartz	18.0%	0.1%	0.8%	1.6%

smallest amounts of mineral phases like pyrite, as this sulfide mineral is likely to bear toxic impurities. This is further discussed in the next section. Quantifications of maps generated by the EFS1-trained classifier (labelled 3 individual mineral maps) are also shown in Table 2 for comparison. Most notably, the 7-mineral trained classifier revealed a new mineral phase presence, dolomite, although this is a phase that was also not captured by previous powder XRD analyses. Further work remains to be done to determine whether dolomite presence is real, however, there is evidence in the literature of dolomite presence in the Eagle Ford shale (Kreisserman and Emmanuel, 2018). Generally, quantifications from all four methodologies presented in Table 2 still agree well in terms of the patterns of carbonate mineral dominance, followed by silicate (quartz) and sulfide mineral presence in the Eagle Ford shale sample.

Abundance quantifications were also done for the vein sample, UW1, and the rock samples, GRS1, NAS1, and HS1 (Table 3). Pixel-by-pixel analyses revealed numerous pixels with multimineral presence, which is expected from fine-grained shales. Minerals such as pyrolusite and quartz in UW1, and GRS1 and NAS1, respectively, were found to be present at negligible amounts. All shale rocks were found to contain significant fractions of carbonate and sulfide minerals, and from this analysis, NAS1 and HS1 were characterized as sulfide rich shales, and GRS1 as a mixed shale. The syntaxial vein UW1 was found to be dominantly carbonate filled, with quartz presence likely to be concentrated in the surrounding rock matrix (Fig. 3h).

4.3. Trace element mapping and quantifications

In this section, we focus on pyrite in the Eagle Ford shale for analysis of trace element presence. After mapping locations of pyrite grains, detailed trace element mapping and quantifications of that mineral phase was possible. The trace element maps, which are now known to be correlated with pyrite, are presented in Fig. 5, along with the maps of two dominant elements in pyrite, iron and sulfur. The maps reveal that pyrite is the most dominant phase to host three important trace elements, arsenic, copper, and zinc, but there is also association of zinc and arsenic with calcite. Such carbonate-metal associations have been observed in nature and as secondary minerals (Costagliola et al., 2013; Hunter et al., 2021), however, spatial correlation of the trace elements is higher with the pyrite phase and this finding is expected as sulfide minerals are the primary ores of these elements (National Research Council, 1977; Ivanov et al., 2020).

With knowledge of the host mineral phase of trace elements, element abundances were calculated for EFS1. XRF intensities were interpreted to reveal abundances of arsenic, zinc, and copper associated with pyrite

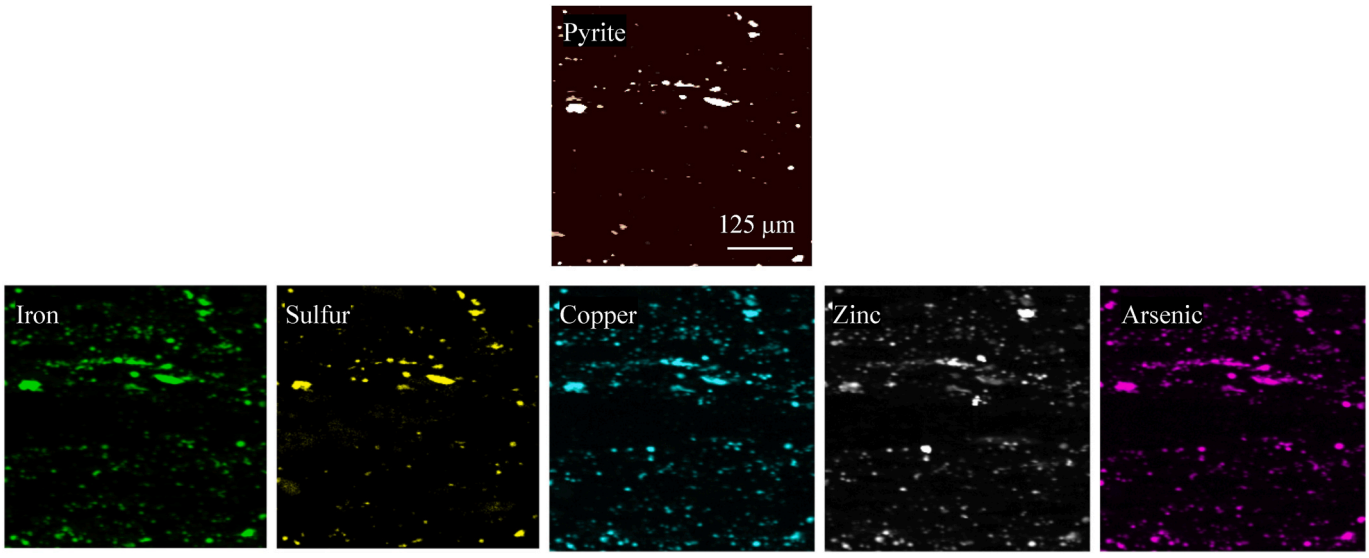

Fig. 5. SMART classifier generated map (500 μm by 500 μm) of pyrite in EFS1 with micron-scale resolution. Also shown in the bottom row are dominant and trace element maps. Black indicates absence.

and calcite. Elemental abundance estimations inform us that pyrite is most enriched in zinc, followed by copper and arsenic. The ternary diagram in Fig. 6 presents the relative abundances of the three elements in each pixel and it is revealed that pyrite pixels are quite heterogeneous in terms of their composition. While the trend in the ternary diagram shows pyrite spots populating the zinc corner, there are still numerous spots where all three elements coexist and the tri-color map of the three elements (Fig. 6) visually captures this heterogeneity. In pyrite, zinc ranged from 0 to 4.2 wt%, arsenic ranged from 0 to 0.05 wt%, and copper ranged from 0 to 0.35 wt%. Concentrations observed in this Eagle Ford shale sample are in fair agreement with observed concentrations of the three elements in other shales; 0.0034–8.8 Zn wt%, 0.0071–0.08 As wt%, and 0.0241–0.708 Cu wt% (Ivanov et al., 2020). Quantifications of the overall trace element weight percent in the calcium carbonate phase revealed negligible maximum weight fraction of zinc, arsenic, and copper at $10^{-2.76}$, $10^{-5.69}$, $10^{-3.67}$ wt%, respectively, further indicating that the majority of the trace metal(loid)s are found in the sulfide phase.

4.4. Size distributions of pyrite and its accessibility

Estimated 3D grain size (diameter) distribution of identified pyrite grains are presented for EFS1 (Fig. 7). Of the total number of pyrite objects identified in the 500 μm by 500 μm cross section, grain size analyses reveal that 62% of the pyrite grains are less than 4 μm in diameter and this phase has a median diameter of 3.17 μm. With the finer resolution of the SMART-based maps, the detectable limit of the pyrite grains is as small as 2.26 μm in diameter. Still, as the shape of the histogram in Fig. 7 suggests, it is likely that pyrite grains in the Eagle Ford shale dominate sizes that are near the detectable limit of this approach. However, this is one of few applications of 2D mineral maps to characterize grain size distributions for pyrite, and estimated values for the diameters are close to reported mean diameters of framboidal pyrite in other shales which range from 3.0 to 6.7 μm in diameter (Liu et al., 2019; Wilkin et al., 1996). This information, coupled with the additional information of accessibility to these small grains, will be valuable to modelers who seek to determine the extent of pyrite's effect on solution chemistry.

To visualize and quantify the surface areas and accessibilities of minerals, adjacency maps for pyrite and calcite in EFS1 were generated

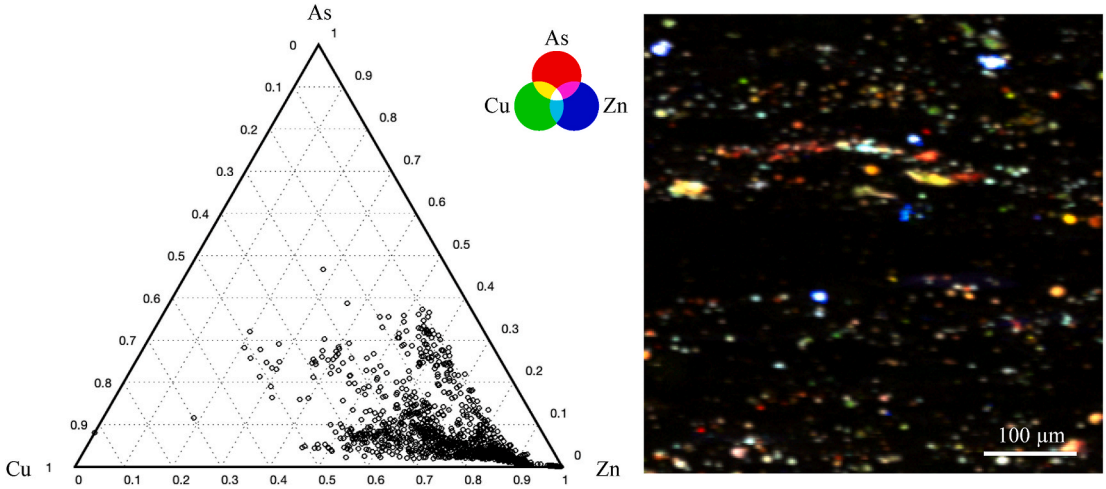

Fig. 6. A ternary plot depicting relative abundances of the three elements, Zn, As, Cu, in pyrite spots in EFS1. Weight percentages were normalized to 1 for graphical representation.

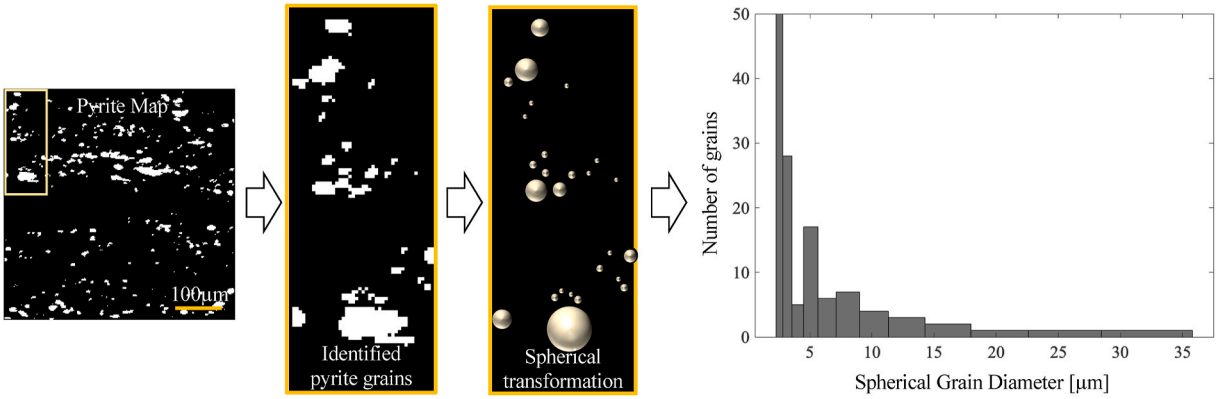

Fig. 7. Histogram of pyrite grain size distribution for the grains identified in the 500 μm by 500 μm EFS1 2D map of pyrite. Objects in the map were transformed to spherical objects based on stereological probabilistic principles.

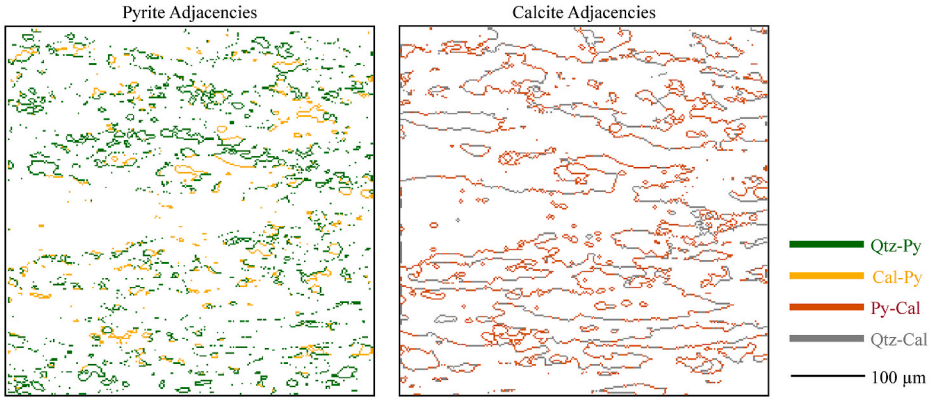

Fig. 8. Adjacency maps of pyrite (left) and calcite (right) in EFS1. Cal-Py corresponds to calcite contacting pyrite (or pyrite contacting calcite), while Qtz-py, Qtz-Cal, and Py-Cal correspond to quartz contacting pyrite, quartz contacting calcite, and pyrite contacting calcite, respectively.

(Fig. 8). These maps are especially useful for visualizing and identifying the pyrite grains deemed more accessible and therefore potentially more mobile or reactive. From qualitative analysis of Fig. 8, it appears that some of the pyrite is fully encased in quartz, although this cannot be known with certainty because of the lack of information in the third dimension. Based on quantitative analyses of the contact line maps, it is estimated that only approximately 28% of the total pyrite surface is adjacent to calcite (Table 4), indicating the remaining surfaces to be in contact with a relatively more stable quartz phase. Whether such a mineral phase needs to be considered in reactive transport modeling is a decision to be made, and adjacency maps can serve as a useful tool to enable these decisions.

The total specific surface area of calcite and pyrite were also estimated, and the values fall within ranges of 0.026–0.04 m^2/g and 0.07–0.1 m^2/g, respectively. Although it is unconventional to report total specific surface area for consolidated rocks (for reasons discussed in section 3.5), these values fall within previously reported Brunauer–Emmett–Teller (BET) derived values for specific surface area accessible by pore space, 0.01–1.1 m^2/g and 0.03–0.5586 m^2/g for calcite and pyrite, respectively (Beckingham et al., 2016 and references therein).

Table 4
Mineral adjacency quantification in EFS1 based on analysis of contact with adjacent minerals, and quantification of total specific surface areas.

	% Pyrite boundaries in contact with	% Calcite boundaries in contact with	Total Specific Surface Area (μm^{-1})	Total Specific Surface Area (m^2/g)
Calcite	28.3%		0.07 to 0.1	0.026 to 0.04
Quartz	71.7%	63.1%		
Pyrite		36.9%	0.35 to 0.50	0.07 to 0.1

5. Conclusions

In this paper, we presented applications of the SMART mineral classifier to generate 2D millimeter-scale maps of minerals for a wide range of natural rock samples by combining μXRF data from different samples. Training data were pooled from two samples to demonstrate the extension of a classifier to predicting a wider suite of minerals, and performance of this updated classifier demonstrated misclassification rates of less than 4% for all minerals. Furthermore, this work highlighted advantages of sub-pixel mineral characterizations, or the ability to identify and quantify multiple minerals per pixel, which is a unique feature of the SMART method yet to be achieved by existing mapping methods. In providing further applications, SMART-generated maps were used to qualitatively and quantitatively to describe mineral reactivity. Mineral maps were coupled to XRF maps of trace elements to define the host minerals of trace elements which could be of environmental concern. This way, the weight percentages of the trace elements could be quantified, and in the EFS1 sample, pyrite was revealed to be the dominant host phase of toxic elements such as zinc (up to 4.2 wt%) and copper. (up to 0.35 wt%). Predictions of expected grain sizes were also done for the pyrite phase in EFS1, as this phase was identified as chemically heterogeneous and distributed throughout the calcite and quartz matrices of the Eagle Ford shale. It was revealed that more than 62% of the pyrite grains are less than 4 μm in diameter, and the shape of the histogram for the size distribution suggests dominance of grains near the detectable limit of grain sizes. Mineral accessibility in this work was

newly defined in terms of adjacency to specific mineral phases, as some minerals are more soluble than others and therefore the evolution of potential pathways to the embedded mineral phase will be different. This is different from the conventional way of defining specific surface area which is done in the context of exposure to pore space. For the two reactive phases in EFS1, calcite and pyrite, total specific surface areas were calculated from analysis of contact with reactive mineral phase(s) and compared to conventional values obtained from analysis of contact with pore space. Results presented in this paper demonstrate ways in which micron-scale 2D mineral maps can be useful for improving characterizations and quantifications of mineral reactivity, and how mineral maps are made especially more valuable via coupling with element maps. Applications of the methodology to a new subset of rock samples of different origin, and incorporation of other relevant mineral phases to existing classifiers remain as future work.

Data availability

Data and computer code are available and accessible on Digital Rocks Portal. See project data branches in Digital Rocks Portal for detailed instructions.

"Eagle Ford Shale: Synchrotron-Based Element and Mineral Maps" (Peters and Kim, 2020). [https://www.digitalrocksportal.org/projects/258].

Declaration of competing interest

The authors declare that they have no known competing financial interests or personal relationships that could have appeared to influence the work reported in this paper.

Acknowledgements

This material is based upon work supported by the High Meadows Environmental Institute at Princeton University. This research used resources of the Advanced Photon Source, a U.S. Department of Energy (DOE) Office of Science User Facility operated for the DOE Office of Science by Argonne National Laboratory under Contract No. DE-AC02-06CH11357. Portions of this work were performed at GeoSoilEnviroCARS (The University of Chicago, Sector 13), Advanced Photon Source (APS), Argonne National Laboratory. GeoSoilEnviroCARS is supported by the National Science Foundation – Earth Sciences (EAR – 1634415) and Department of Energy- GeoSciences (DE-FG02-94ER14466). We acknowledge Dr. Jeffery Fitts for doing the micro-XRF scans of the Green River shale, Haynesville shale, and New Albany shale.

Appendix A. Supplementary data

Supplementary data to this article can be found online at https://doi.org/10.1016/j.apgeochem.2021.105162.

References

Asadi, P., Beckingham, L.E., 2021. Integrating machine/deep learning methods and filtering techniques for reliable mineral phase segmentation of 3D X-ray computed tomography images. Energies 14, 4595. https://doi.org/10.3390/en14154595.

Baek, S.H., Hong, J.W., Kim, K.Y., Yeom, S., Kwon, T.H., 2019. X-ray computed microtomography imaging of abiotic carbonate precipitation in porous media from a supersaturated solution: insights into effect of CO2 mineral trapping on permeability. Water Resour. Res. 55, 3835–3855. https://doi.org/10.1029/2018WR023578.

Beckingham, L.E., Mitnick, E.H., Steefel, C.I., Zhang, S., Voltolini, M., Swift, A.M., Yang, L., Cole, D.R., Sheets, J.M., Ajo-Franklin, J.B., DePaolo, D.J., Mito, S., Xue, Z., 2016. Evaluation of mineral reactive surface area estimates for prediction of reactivity of a multi-mineral sediment. Geochem. Cosmochim. Acta 188, 310–329. https://doi.org/10.1016/j.gca.2016.05.040.

Crandell, L.E., Peters, C.A., Um, W., Jones, K.W., Lindquist, W.B., 2012. Changes in the pore network structure of Hanford sediment after reaction with caustic tank wastes. J. Contam. Hydrol. 131, 89–99. https://doi.org/10.1016/j.jconhyd.2012.02.002.

Costagliola, P., Bardelli, F., Benvenuti, M., Di Benedetto, F., Lattanzi, P., Romanelli, M., Paolieri, M., Rimondi, V., Vaggelli, G., 2013. Arsenic-bearing calcite in natural travertines: evidence from sequential extraction, μxAS, and μxRF. Environ. Sci. Technol. 47, 6231–6238. https://doi.org/10.1021/es304953a.

Deng, H., Fitts, J.P., Tappero, R.V., Kim, J.J., Peters, C.A., 2020. Acid erosion of carbonate fractures and accessibility of arsenic-bearing minerals: in operando synchrotron-based microfluidic experiment. Environ. Sci. Technol. 54, 12502–12510. https://doi.org/10.1021/acs.est.0c03736.

Deng, H., Navarre-Sitchler, A., Heil, E., Peters, C., 2021. Addressing water and energy challenges with reactive transport modeling. Environ. Eng. Sci. 38, 109–114. https://doi.org/10.1089/ees.2021.0009.

Ellis, B.R., Peters, C.A., 2016. 3D Mapping of calcite and a demonstration of its relevance to permeability evolution in reactive fractures. Adv. Water Resour. 95, 246–253. https://doi.org/10.1016/j.advwatres.2015.07.023.

Glassley, W.E., Simmons, A.M., Kercher, J.R., 2002. Mineralogical heterogeneity in fractured, porous media and its representation in reactive transport models. Appl. Geochem. 17, 699–708. https://doi.org/10.1016/S0883-2927(02)00031-8.

Glynn, P.D., Reardon, E.J., Plummer, L.N., Busenberg, E., 1990. Reaction paths and equilibrium end-points in solid-solution aqueous-solution systems. Geochile 54, 267–282.

Hunter, H.A., Ling, F.T., Peters, C.A., 2020. Metals coprecipitation with barite: nano-XRF observation of enhanced strontium incorporation. Environ. Eng. Sci. 37, 235–245. https://doi.org/10.1089/ees.2019.0447.

Hunter, H.A., Ling, F.T., Peters, C.A., 2021. Coprecipitation of heavy metals in calcium carbonate from coal fly ash leachate. ACS ES&T Water 1, 339–345. https://doi.org/10.1021/acsestwater.0c00109.

Ivanov, K.S., Maslennikov, V.V., Artemyev, D.A., Tseluiko, A.S., 2020. Highly metalliferous potential of framboidal and nodular pyrite varieties from the oil-bearing jurassic bazhenov formation, Western Siberia. Minerals 10, 1–24. https://doi.org/10.3390/min10050449.

Kim, J.J., Ling, F.T., Plattenberger, D.A., Clarens, A.F., Lanzirotti, A., Newville, M., Peters, C.A., 2021. SMART mineral mapping: synchrotron-based machine learning approach for 2D characterization with coupled micro XRF-XRD. Comput. Geosci. 156, 104898. https://doi.org/10.1016/j.cageo.2021.104898.

Kreisserman, Y., Emmanuel, S., 2018. Release of particulate iron sulfide during shale-fluid interaction. Environ. Sci. Technol. 52, 638–643. https://doi.org/10.1021/acs.est.7b05350.

Lai, P., Moulton, K., Krevor, S., 2015. Pore-scale heterogeneity in the mineral distribution and reactive surface area of porous rocks. Chem. Geol. 411, 260–273. https://doi.org/10.1016/j.chemgeo.2015.07.010.

Landrot, G., Ajo-Franklin, J.B., Yang, L., Cabrini, S., Steefel, C.I., 2012. Measurement of accessible reactive surface area in a sandstone, with application to CO 2 mineralization. Chem. Geol. 318–319, 113–125. https://doi.org/10.1016/j.chemgeo.2012.05.010.

Lanzirotti, A., Newville, M., Manoukian, L., Lange, K., 2016. High-speed, Coupled Micro-beam XRD/XRF/XAFS Mapping at GSECARS. https://doi.org/10.1346/cms-wls-21.5. APS Beamline 13-ID-E 21, 53–64.

Li, L., Peters, C.A., Celia, M.A., 2007. Effects of mineral spatial distribution on reaction rates in porous media. Water Resour. Res. 43, 1–17. https://doi.org/10.1029/2005WR004848.

Li, L., Peters, C.A., Celia, M.A., 2006. Upscaling geochemical reaction rates using pore-scale network modeling. Adv. Water Resour. 29, 1351–1370. https://doi.org/10.1016/j.advwatres.2005.10.011.

Ling, F.T., Hunter, H.A., Fitts, J.P., Peters, C.A., Acerbo, A.S., Huang, X., Yan, H., Nazaretski, E., Chu, Y.S., 2018. Nanospectroscopy captures nanoscale compositional zonation in barite solid solutions. Sci. Rep. 8, 1–11. https://doi.org/10.1038/s41598-018-31335-3.

Liu, M., Shabaninejad, M., Mostaghimi, P., 2017. Impact of mineralogical heterogeneity on reactive transport modelling. Comput. Geosci. 104, 12–19. https://doi.org/10.1016/j.cageo.2017.03.020.

Liu, Z., Chen, D., Zhang, J., Lü, X., Wang, Z., Liao, W., Shi, X., Tang, J., Xie, G., 2019. Pyrite morphology as an indicator of paleoredox conditions and shale gas content of the Longmaxi and Wufeng shales in the middle Yangtze area, South China. Minerals 9. https://doi.org/10.3390/min9070428.

Ma, J., Ahkami, M., Saar, M.O., Kong, X.Z., 2021. Quantification of mineral accessible surface area and flow-dependent fluid-mineral reactivity at the pore scale. Chem. Geol. 563, 120042. https://doi.org/10.1016/j.chemgeo.2020.120042.

National Research Council (US), 1977. Committee on Medical and Biological Effects of Environmental Pollutants. Arsenic: Medical and Biologic Effects of Environmental Pollutants. National Academies Press (US), Washington (DC), p. 3, 1977, Distribution of Arsenic in the Environment. Available from: https://www.ncbi.nlm.nih.gov/books/NBK231016/.

Newville, M., 2013. Larch: an analysis package for XAFS and related spectroscopies. J. Phys. Conf. 430 https://doi.org/10.1088/1742-6596/430/1/012007, 012007, 2.

Peters, C.A., 2009. Accessibilities of reactive minerals in consolidated sedimentary rock: an imaging study of three sandstones. Chem. Geol. 265, 198–208. https://doi.org/10.1016/j.chemgeo.2008.11.014.

Peters, C.A., Hajirezaie, S., Kim, J.J., Crandall, D., 2021. Mineralized Fracture in a Mudrock Shale. https://doi.org/10.17612/P4WH-W011. Digital Rocks Portal.

Peters, C.A., Kim, J.J., 2020. Eagle Ford Shale: Synchrotron-Based Element and Mineral Maps. https://doi.org/10.17612/T3A6-6356. Digital Rocks Portal.

Qin, F., Beckingham, L.E., 2021. The impact of mineral reactive surface area variation on simulated mineral reactions and reaction rates. Appl. Geochem. 124, 104852. https://doi.org/10.1016/j.apgeochem.2020.104852.

Sahagian, D.L., Proussevitch, A.A., 1998. 3D particle size distributions from 2D observations: stereology for natural applications. J. Volcanol. Geoth. Res. 84, 173–196. https://doi.org/10.1016/S0377-0273(98)00043-2.

Spokas, K., Fang, Y., Fitts, J.P., Peters, C.A., Elsworth, D., 2019. Collapse of reacted fracture surface decreases permeability and frictional strength. J. Geophys. Res. Solid Earth 124, 12799–12811. https://doi.org/10.1029/2019JB017805.

Spokas, K., Peters, C.A., Pyrak-Nolte, L., 2018. Influence of rock mineralogy on reactive fracture evolution in carbonate-rich caprocks. Environ. Sci. Technol. 52, 10144–10152. https://doi.org/10.1021/acs.est.8b01021.

Sutton, S.R., Lanzirotti, A., Newville, M., Rivers, M.L., Eng, P., Lefticariu, L., 2017. Spatially resolved elemental analysis, spectroscopy and diffraction at the GSECARS sector at the advanced Photon source. J. Environ. Qual. 46, 1158–1165. https://doi.org/10.2134/jeq2016.10.0401.

Weibel, E.R., 1989. Measuring through the microscope: development and evolution of stereological methods. J. Microsc. 155, 393–403. https://doi.org/10.1111/j.1365-2818.1989.tb02898.x.

Wilkin, R.T., Barnes, H.L., Brantley, S.L., 1996. The size distribution of framboidal pyrite in modern sediments: an indicator of redox conditions. Geochem. Cosmochim. Acta 60, 3897–3912. https://doi.org/10.1016/0016-7037(96)00209-8.

Zhang, L., Parthasarathy, H., Karamalidis, A., 2017. Investigation on arsenopyrite dissolution and as (III) migration under geologic carbon storage conditions: a numerical simulation approach. Greenh. Gases Sci. Technol. 7, 460–473. https://doi.org/10.1002/ghg.1651.